AGU ADVANCING EARTH AND SPACE SCIENCE

Space Weather

RESEARCH ARTICLE
10.1029/2021SW002787

Multi-Year Statistics of LEO Energetic Electrons as Observed by the Korean NextSat-1

Jaeheung Park[1,2], Kyoung Wook Min[3], Hoonkyu Seo[4], Eo-Jin Kim[5], Kwangsun Ryu[4], Jongdae Sohn[1], Jongho Seon[6], Ji-Hyeon Yoo[7], Seunguk Lee[7], Brian Kress[8], Junchan Lee[4], Changho Woo[4], and Dae-Young Lee[7]

[1]Space Science Division, Korea Astronomy and Space Science Institute, Daejeon, South Korea, [2]Department of Astronomy and Space Science, Korea University of Science and Technology, Daejeon, South Korea, [3]Department of Physics, Korea Advanced Institute of Science and Technology, Daejeon, South Korea, [4]Satellite Technology Research Center, Korea Advanced Institute of Science and Technology, Daejeon, South Korea, [5]Korea Institute of S&T Evaluation and Planning, Chungcheongbuk-do, South Korea, [6]School of Space Research, Kyung Hee University, Yongin, South Korea, [7]Department of Astronomy and Space Science, Chungbuk National University, Cheongju, South Korea, [8]National Centers for Environmental Information, NOAA/NESDIS/NCEI, Boulder, CO, USA

Key Points:

- Energetic electron flux measured by Next-Generation Small Satellite-1 (NextSat-1) exhibits a positive correlation to Geostationary Operational Environmental Satellite 17 observations, with the regression slope of 1 ~ 2.5
- The power spectral indices estimated from NextSat-1 electron data conform to those of geosynchronous observations and with previous studies
- Even for the electrons near the loss cone edge, the slot-region outer edge moves inward with increasing geomagnetic activity

Correspondence to:
J. Park,
pj@kasi.re.kr

Citation:
Park, J., Min, K. W., Seo, H., Kim, E.-J., Ryu, K., Sohn, J., et al. (2021). Multi-year statistics of LEO energetic electrons as observed by the Korean NextSat-1. *Space Weather*, *19*, e2021SW002787. https://doi.org/10.1029/2021SW002787

Received 19 APR 2021
Accepted 19 JUL 2021

Abstract Monitoring the Earth's radiation belt by Low-Earth-Orbit (LEO) satellites has a long history and complemented observations near the high-altitude equatorial plane. However, most of the previous LEO missions suffered from limitations in energy resolution, energy range, *L*-shell coverage, or the mission lifetime, which leave room for further improvement in this topic. For <80 keV electrons, the slot-region outer edge at LEO moves inward with increasing geomagnetic activity, which agrees with previous Van Allen Probes reports. The behavior is more conspicuous for lower-energy electrons. Latitudinal profiles of outer-belt electron flux are smoother equatorward of the geosynchronous footprint latitudes (|MLAT| ~ 66°) than poleward. The NextSat-1 electron flux is positively correlated to geosynchronous observations, with the coefficient generally higher for higher electron energies. Also, both the geosynchronous and NextSat-1 data exhibit similar spectral indices close to −3 in the log-log space. All these results complement and expand previous knowledge on energetic electrons. The main findings are discussed in the context of existing literature.

Plain Language Summary The Earth's radiation belt consists of energetic particles which can potentially harm space assets and astronauts. Radiation belt science has a long history since the first discovery in the 1950s, and many of the unanswered questions were solved during the Van Allen Probes (VAP) era between 2012 and 2019. However, after the decommissioning of VAP, only a few spacecraft are continuously monitoring the radiation belt. In this study, we introduce the energetic electron data produced by a Korean Low-Earth-Orbit satellite, NextSat-1. Since 2019, the satellite measures electron flux in the energy range between ~30 keV and ~2 MeV, at an altitude of 575 km and a local time of 22:30. We compare the data to geosynchronous GOES-17 observations and find a good correlation between their daily variations (correlation coefficients > 0.6) and reasonable agreement in their power spectral index ranges (between −3.0 and −3.5). NextSat-1 expands existing knowledge obtained from Medium-Earth-Orbit data, such as the inner edge of the outer radiation belt changing with geomagnetic activity and energy. We discuss those findings in the context of previous studies.

1. Introduction

The terrestrial radiation belt was first discovered by Explorer-1 launched in 1958 (Van Allen and Frank, 1959). The climatological variations of the belt have been studied for a long time because the high-energy particles therein have both scientific and socio-economic significance. For example, electronics onboard artificial satellites can be damaged by those particles, which leads to spacecraft anomaly or even total loss (e.g., Choi et al., 2011). Careful analyses of the radiation belt climatology can help mitigate economic loss, either by changing satellites' operational scenarios in an emergency or by adopting radiation-tolerant designs during the spacecraft manufacture (e.g., https://en.wikipedia.org/wiki/Juno_Radiation_Vault).

The radiation belts have been probed by Low-Earth-Orbit (LEO; heights below 2,000 km) and magnetospheric (e.g., Medium-Earth Orbit and Geosynchronous Orbit) satellites, both of which have their own

merits and demerits. Satellites at high altitudes near the equatorial plane can directly access the regions containing a majority of the radiation belt particles. In exchange, the onboard instruments should have extremely high pitch angle resolution to resolve the populations near the loss cone. For most of the previous missions, however, the resolution was too coarse to distinguish particles right outside and inside the loss cone. In general, the magnetospheric missions could cover a limited range of *L*-shells: For example, Van Allen Probes (e.g., Kessel et al., 2013; Mauk et al., 2012; Reeves et al., 2016) were restricted inside the geosynchronous orbit. Furthermore, the slow orbital speed inherently leads to the time-space aliasing of the observations: We cannot clearly tell whether observed electron flux changes are caused by temporal or spatial variations. On the other hand, LEO observations can discriminate electron populations just outside and inside the loss cone. It takes only ∼25 min for LEO satellites to scan through the whole *L*-shells once: Their fast orbital speed (∼7.5 km/s) is beneficial to disentangling time-space ambiguity for the phenomena having time scales larger than about 25 min. However, the LEO satellites cannot get information on the equatorially trapped energetic particles, which actually constitute the dominant population of the radiation belt. Hence, the LEO and magnetospheric missions complement each other.

Since the 1990s, many LEO missions have monitored the radiation belt: the Solar, Anomalous, Magnetospheric Particle Explorer (SAMPEX), Polar Orbiting Environmental Satellites (POES), Detection of Electro-Magnetic Emissions Transmitted from Earthquake Regions (DEMETER), and Science and Technology Satellite-1 (STSAT-1) to name a few. In recent years, nanosatellites have also joined this field (e.g., Capannolo et al., 2021) and are actively monitoring the LEO radiation belt. However, there is still room for further improvement from the existing studies and missions. For instance, SAMPEX had only a limited number of energy channels (Selesnick, 2015, Figure 2; Blum et al., 2015, Section 2) and concomitantly coarse energy resolution. POES satellites also have only a few integral energy channels for electron measurements, each of which measures integrated particle flux above a fixed threshold energy. DEMETER (Sauvaud et al., 2006) rarely operated at high latitudes corresponding to $L > 6$ (Whittaker et al., 2013, Figure 1). STSAT-1 had high sampling rate and energy resolution, but a limited energy range (0.1∼0.4 MeV): see Lee et al. (2005, 2011). Most of the nanosatellites launched by far have short lifetimes (usually less than 1 year) and are inappropriate for long-term statistical studies.

As a result, it is still worth observing LEO energetic particles by an instrument with fine energy resolution, seamlessly over a wide *L*-shell range for a long period. This is the niche market yet to be exploited and the rationale of the new Korean mission that we will address throughout this paper. In the following Section 2 we briefly describe the spacecraft and instruments used in this study as well as the data processing methods. In Section 3, statistical analyses of the observations are presented, and their key features are discussed. In Section 4 we address additional features of the observed energetic electrons in the context of previous studies. A number of caveats for data quality of the new Korean mission are also given in that section. Lastly, Section 5 summarizes the main findings and draws conclusions.

2. Instruments and Data Processing Methods

The Next-Generation Small Satellite-1 (NextSat-1) is a Korean micro-satellite (∼100 kg) mission dedicated to astrophysics and space sciences. The satellite was launched from the Vandenberg Air Force Base on December 03, 2018. The orbit is Sun-synchronous at 575 km above ground and 10:30–22:30 local time (LT). The main payload is the Near-infrared Imaging Spectrometer for Star formation history (NISS), which takes images of the universe in the near-infrared spectral range (Jeong et al., 2014). The secondary payload, the Instrument for the Study of Space Storms (ISSS), provides information on high-energy particles (Seo et al., 2015, 2021; Sohn et al., 2018) and parameters of background cold ionospheric plasma (Lee et al., 2018). The ISSS data are supplemented by a navigation-grade flux-gate magnetometer (FGM), which can continuously measure magnetic field vectors. In this study, we focus on the energetic electron flux measured by the onboard High-Energy Particle Detector (HEPD) and Medium-Energy Particle Detector (MEPD). Details of the instrumentation and initial operation results of the NextSat-1/ISSS are available at Choi et al. (2014), Kim et al. (2020), and Yoo et al. (2021): see also http://n1isss.kaist.ac.kr/02_02.php. Some of their key features are briefly summarized below.

The MEPD measures energetic particles in the energy range of 0.012 ~ 0.4 MeV. Usually, the observations are taken at 64 quasi-logarithmic energy steps. MEPD has two telescopes, each of which has a 2-dimensional field-of-view (FOV) of 15° by 70°. In normal operation, MEPD-A and MEPD-B point along and perpendicular to magnetic field direction, respectively: This attitude control allows the former and the latter to measure locally precipitating and trapped particles. Each telescope consists of four independent Silicon detectors behind an electrostatic deflector. As a result, the 2 center detectors of MEPD (DET1 and DET2) can respond to neutral particles while the other two measure electrons (DET0) and ions (DET3), respectively. In this study, we will use the electron flux from Detector 0 (DET0) of MEPD-A and MEPD-B.

HEPD is also a Silicon-based particle detector for charged particles, but has a target energy range higher than that of MEPD: for example, from 0.4 to 1.8 MeV for electrons. The HEPD has three telescopes, two of which are directed parallel (T0) and perpendicular (T2) to the local geomagnetic field. The remaining telescope (T1) has a pointing direction in-between (i.e., ~45° away from the magnetic zenith). The cone angle of the HEPD FOV is 33.4°. An Aluminum foil at the entrance of HEPD (thickness ~ 45 μm) blocks <2 MeV protons (http://n1isss.kaist.ac.kr/02_02.php), which helps HEPD discriminate electrons and ions at similar energy ranges. We use the electron flux data for this study.

Both the MEPD and HEPD mainly operate on the nightside (~2230 LT) in both hemispheres, where the spacecraft is not Sun-pointing, but aligns the attitude along the geomagnetic field lines. As the operations are generally restricted to eclipse (dark) periods, most of the data during solstices come from the winter hemisphere: that is, in the Southern Hemisphere (SH) around June solstice and in the Northern Hemisphere (NH) during December Solstice. For statistical analyses, we use MEPD and HEPD data obtained from January 2019 to February 2021. However, MEPD data during earlier periods (the year 2019) are not used because the instrument settings were not fully settled down at that time.

There are a number of caveats using the LEO electron counts, such as given by NextSat-1/ISSS, for radiation belt studies. First, energetic electron observations at LEO can only represent the populations near the loss cone. Locally trapped electrons observed at LEO are near the edge of the loss cone while locally precipitating ones are deep inside the loss cone: see Reidy et al. (2021, Figure 3). In terms of equatorial pitch angles, both locally trapped and precipitating populations are only a few degrees away from the magnetic nadir (i.e., equatorial pitch angle = 0°). Second, as the spacecraft altitude is nearly fixed (~575 km), in the following discussions we use the absolute value of magnetic latitude (|MLAT|) interchangeably with the *L*-shell unless stated otherwise. Throughout this paper, the MLAT is the Quasi-Dipole latitude (e.g., Laundal and Richmond, 2017) calculated for the actual spacecraft altitude plus the reference Earth's radius of 6,371.2 km. The Quasi-Dipole latitude is estimated by (a) tracking up along realistic geomagnetic field lines (e.g., those from the international geomagnetic reference field) from the spacecraft position to the equatorial plane, and (b) then tracking down along the idealized dipole field line to a reference altitude. This coordinate system is frequently used in LEO data analyses (e.g., De Michelis et al., 2021). Details of the coordinates are given in Laundal and Richmond (2017).

The MEPD and HEPD data are screened by the following criteria. First, we remove all the data from the South Atlantic Anomaly (SAA) region to avoid cross-contamination from ions to electrons (e.g., Fennell et al., 2015; Li et al., 2013). Here we conservatively define the SAA as the region where the magnetic field strength recorded by the NextSat-1/FGM is smaller than 30,000 nT. Second, we neglect the MEPD and HEPD data obtained under uncontrolled attitudes. Specifically, we impose the following condition: $\left|B_x\right| \geq 5.7 \times \sqrt{B_y^2 + B_z^2}$, where B_x, B_y, and B_z are the *x*-, *y*-, and *z*-components of the geomagnetic field in the spacecraft coordinate system, which is fixed to the satellite body. Note that MEPD-A and HEPD-T0, both of which are to measure locally precipitating electrons, are aligned with the *x*-axis of the spacecraft coordinate system. This condition constrains the MEPD-A and HEPD-T0 center axis alignment to within ±10° of the magnetic field direction. As for MEPD, we restrict the energy range of MEPD to 0.03 ~ 0.08 MeV, the reason for which will be detailed in Section 4.

Ap indices (https://www.gfz-potsdam.de/en/kp-index/related-indices/) are used as a proxy for geomagnetic disturbances in this study. Specifically, Ap index of 10 is used as a borderline between quiet and disturbed conditions. The indices are available at the National Aeronautics and Space Administration OMNIWeb (https://omniweb.gsfc.nasa.gov/).

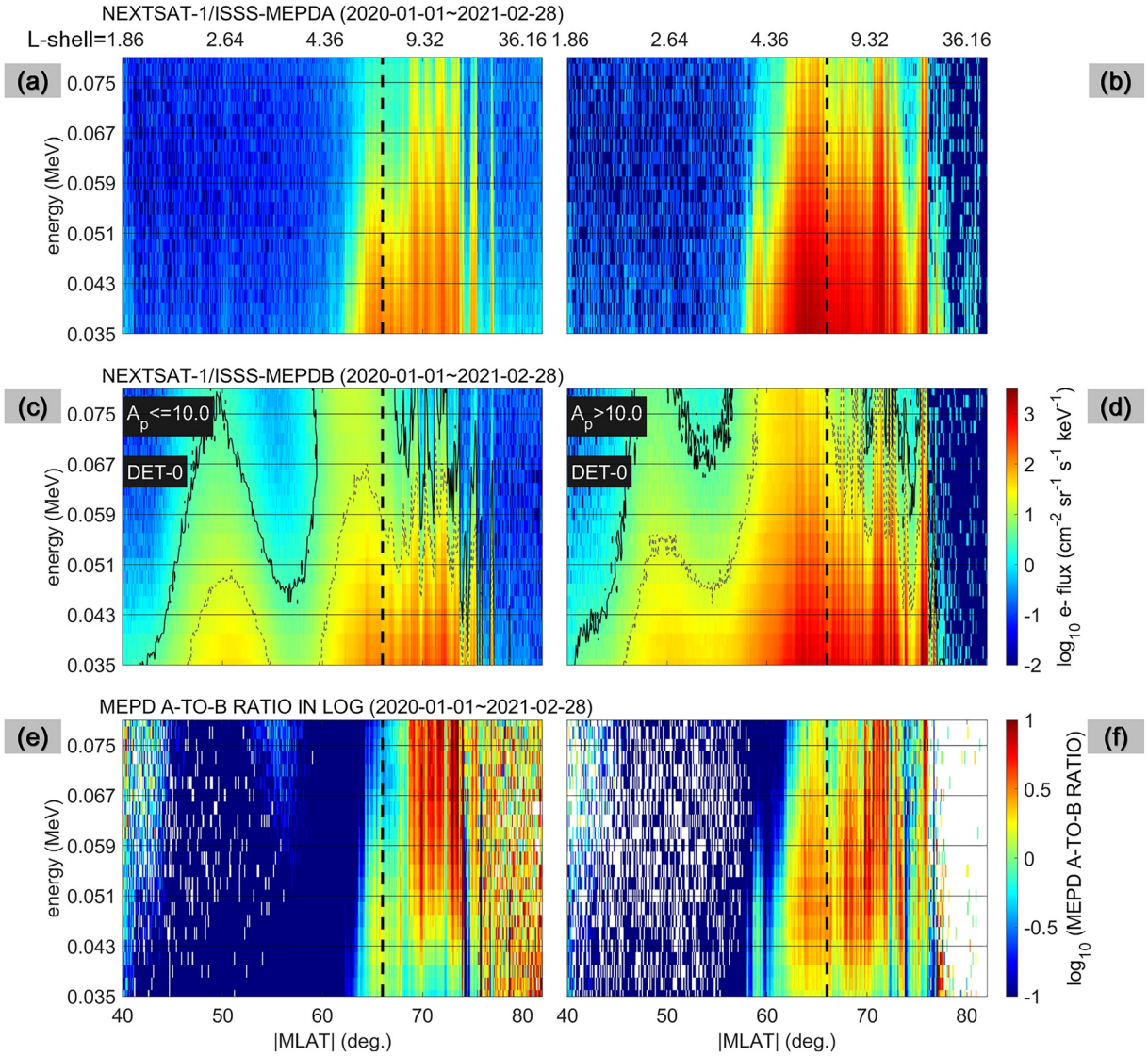

Figure 1. Sub-MeV electron flux measured by the Next-Generation Small Satellite-1/Medium-Energy Particle Detector and bin-averaged a function of magnetic latitude (|MLAT|) and energy. Approximate dipole *L*-shells corresponding to the quasi-dipole |MLAT| are shown at the top of the top row. The top and middle rows represent locally precipitating and trapped electrons, respectively. The bottom row shows the ratio between the top and middle rows in a logarithmic color scale. The left and right columns correspond to geomagnetically quiet and disturbed periods, in that order. The thick black vertical dashed lines represent |MLAT|~66°, which is approximately conjugate to the geosynchronous orbit. Thin solid black and gray dashed contours are given to guide readers' eyes.

3. Results

3.1. Slot Region Edges Dependent on Energy, Geomagnetic Activity, and Pitch Angles

Figure 1 presents the medium-energy electron flux observed by NextSat-1/MEPD, as a function of |MLAT| (abscissa) and energy (ordinate). Approximate dipole *L*-shell values, which are calculated by Lühr and Xiong (2010, Equation 3) with Quasi-Dipole MLAT, are given on the top of the top row. The top and middle rows respectively correspond to locally precipitating (MEPD-A; panels a–b) and locally trapped (MEPD-B; panels c–d) populations. The bottom row (panels e–f) shows the ratio between the MEPD-A and MEPD-B fluxes in a logarithmic scale. The left and right columns represent geomagnetically quiet (Ap ≤ 10) and disturbed (Ap > 10) periods, respectively. The vertical black dashed lines at |MLAT| = 66° represent the nominal footprint of geosynchronous orbit mapped along geomagnetic field lines.

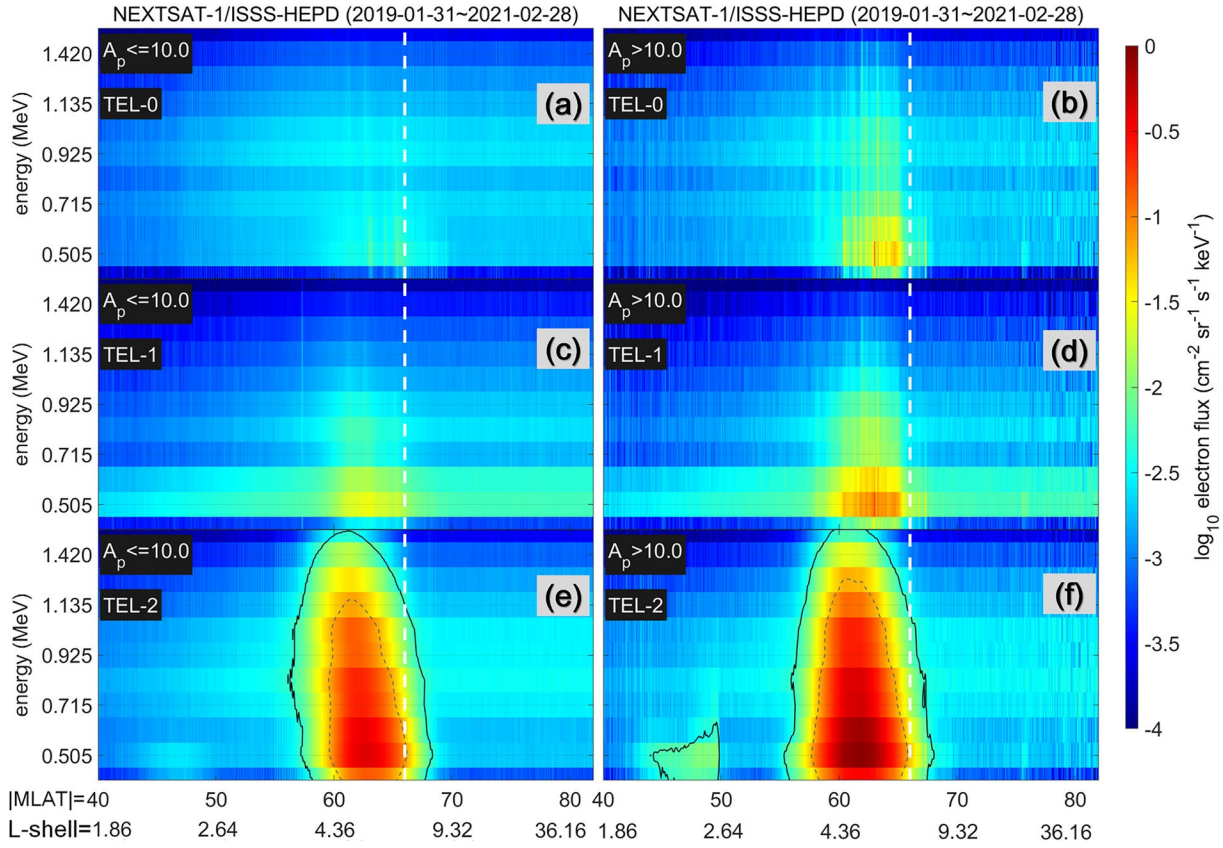

Figure 2. Sub-MeV and MeV electron flux measured by the Next-Generation Small Satellite-1/High-Energy Particle Detector as a function of magnetic latitude (|MLAT|) and energy. Below the horizontal (MLAT) axes, approximate dipole *L*-shells corresponding to the quasi-dipole |MLAT| are given. Each row from top to bottom represents locally precipitating, intermediate, and trapped electrons, in that order. Similar to Figure 1, the left and right columns correspond to geomagnetically quiet and disturbed periods, respectively. The thick white dashed vertical lines represent the nominal footprint of the geosynchronous orbit. Thin solid black and gray dashed contours are presented for guiding readers' eyes onto the shapes of the slot region edge.

In Figures 1c and 1d, the most notable feature is the shape of the slot region around |MLAT| = 50° ~ 60°, which is nearly void of energetic electrons. Thin solid black and gray dashed contours are given to guide readers' eyes onto the general shapes of the slot regions. During geomagnetically quiet periods (Figure 1c), the slot region is clearly identifiable, and its outer edge is generally steep. The slot center is at slightly lower |MLAT| for higher energy channels. On the contrary, during geomagnetic disturbances (Figure 1d), the slot is significantly filled with electrons, especially for low-energy channels (e.g., <0.05 MeV). For locally precipitating populations (Figures 1a and 1b; MEPD-A), the outer edge of the slot region also moves inward with increasing Ap, but the Ap-dependent slot-region filling is not as conspicuous as for the locally trapped population. Precipitating electrons in the inner belt is extremely weak, and the strength does not clearly depend on Ap indices. Figures 1e and 1f confirm the weakness (bluish color) of the inner-belt electron precipitations. In the outer belt, the ratio becomes larger than unity (reddish color) for a portion of the energy-|MLAT| space, to which we will come back in Section 4.

Figure 2 presents the electron flux of NextSat-1/HEPD in a similar format to those of Figures 1a–1d, but for three different pitch angles. From top to bottom, they respectively correspond to locally precipitating (HEPD-T0), intermediate (HEPD-T1), and locally trapped (HEPD-T2) populations. Note that the electron energy range of Figure 2 (HEPD) is higher than that of Figure 1 (MEPD). The lowest energy channel of HEPD (~0.4 MeV) exhibits lower flux than the second-lowest, which can be attributed to the reference voltage of the electronics for avoiding the noise floor: The lowest energy channel will be omitted from the discussions given below. Figures 2e and 2f (HEPD-T2, i.e., the locally trapped populations) generally support the Ap-dependent shapes of the slot region presented by Figure 1. For high Ap (Figure 2f), the outer (i.e., higher-|MLAT|) edge of the slot region (contour lines for a visual guide) runs from low |MLAT| and

low energy toward high |MLAT| and high energy. For low Ap (Figure 2e), the contour lines near the slot region's outer edge are nearly vertical or C-shaped. Above ∼1 MeV, the outer edge of the slot region has similar tilt directions for both quiet (Figure 2e) and disturbed (Figure 2f) geomagnetic conditions while they are different below ∼0.8 MeV. As in Figure 1, for the locally precipitating electrons (HEPD-T0; Figures 2a and 2b), the Ap dependence of the slot region shape is not conspicuous, and the inner belt is nearly void. Note in Figure 2 that the locally precipitating electron fluxes (panels a–b) are much weaker than the locally trapped ones (panels e–f). Electrons with intermediate pitch angles (T1: Figures 2c and 2d) exhibit behavior halfway between those of locally trapped (T2) and precipitating (T0) populations. Note that horizontal band-like structures in pale blue color spanning a wide |MLAT| range seem to be artifacts: for example, around 0.8 MeV for Telescope-2 (Figures 2e and 2f) and below 0.6 MeV for Telescope-1 (Figures 2c and 2d). These artifacts will be discussed later in Section 4.

In Figures 1 and 2, the slot region shapes for locally trapped electrons (Figures 1c–1d and Figures 2e and 2f) agree with previous observations by the Van Allen Probes (VAP): see Reeves et al. (2016) and Ripoll et al. (2016). Those two papers reported that low-energy (<1 MeV) electron flux varies significantly with geomagnetic activity. During geomagnetic disturbances, the low-energy electrons are injected inwards from the outer space (i.e., from higher L-shells or equivalently from higher |MLAT| in Figures 1 and 2). The consequence is a clearly V-shaped slot region in the L-energy space (or equivalently, |MLAT|-energy space in Figures 1 and 2). During quiet periods, those low-energy electrons are quickly removed toward the ground by plasmaspheric hiss waves, which restore the slot region's pre-disturbance, nearly vertical or C-like shapes in the |MLAT|-energy space. High-energy (>1 MeV) electrons are relatively less affected by the geomagnetic disturbance and nearly keep the same structure irrespective of geomagnetic activity (e.g., Reeves et al., 2016, Figure 11): This feature agrees well with our Figures 2e and 2f.

Though the NextSat-1 observations in Figures 1c, 1d, 2e and 2f nearly reproduce the VAP data shown in Reeves et al. (2016) and Ripoll et al. (2016), our Figures 1 and 2 still give additional information that can complement existing knowledge. First, the VAP data are generally dominated by equatorially trapped electrons (i.e., electrons with high equatorial pitch angles). As a result, it was not explicitly evidenced before whether the dependences of the slot region shape on geomagnetic disturbance, as reported by Reeves et al. (2016), remain valid for electrons with low equatorial pitch angles (i.e., near the loss cone edge). Figures 1 and 2 demonstrate that the relationship reported by Reeves et al. (2016) and Ripoll et al. (2016) remain largely valid just outside the edge of the loss cone (i.e., for locally trapped electrons at LEO), but the trend is not as clear deep inside the loss cone (i.e., for locally precipitating electrons at LEO).

3.2. Smoothness of the |MLAT| Profiles: Inside Versus Outside the Geosynchronous Footprints

The MEPD observations in Figure 1 provide information on the latitudinal smoothness of electron flux distributions. For both locally trapped (MEPD-B; Figures 1c and 1d) and precipitating (MEPD-A; Figures 1a and 1b) populations and for both geomagnetically quiet and disturbed periods, the latitudinal profiles are generally smoother inside the geosynchronous footprints (i.e., leftward of the thick vertical dashed lines) than outside. Note that Figure 1 represents a statistical distribution of electron flux, which is based on >1-year or NextSat-1/MEPD observations. Higher-energy electrons observed by HEPD (Figure 2) are mostly confined inside the geosynchronous footprints, and it is difficult to compare the radial profiles inside and outside of the |MLAT|.

This result is as expected from the consensus that (a) sub-MeV electrons are frequently injected inwards from the outer magnetosphere while higher L-shells are more vulnerable to such injections than lower L-shells (e.g., Turner et al., 2015), (b) convection electric field, which can affect electron trajectories, is more variable at higher L-shells (e.g., Khazanov et al., 2004, Figure 3), and (c) trapped populations are in general rare at L-shells outside the geosynchronous orbit (Li et al., 2010, Figures 4–6). We can expect that these three points lead to less smooth electron profiles outside the geosynchronous L-shells than inside. Our results can be nevertheless meaningful because the smoothness of electron |MLAT| (or L-shell) profiles is observed seamlessly by a single satellite over a wide L-shell range. Most of the previous studies had a limited L-shell coverage. For example, the VAP observations were only inside the geosynchronous orbit while there were endeavors to extend the limit by combining the data with the Time History of Events and Macroscale Interactions during Substorms data (Boyd et al., 2018, Figure 2; Xiang et al., 2016, Figures 6 and 7)

or geosynchronous data (e.g., Turner et al., 2015). The DEMETER satellite at LEO conducted extensive observations of energetic particles, but the extent rarely reached poleward of |MLAT|>66°. Several papers presented *L*-shell profiles of sub-MeV electron flux across a wide *L*-shell range: For example, Shin et al. (2014, Figure 2) in the magnetosphere and Xiang et al. (2016, Figure 5) and Kim et al. (2016) at LEO. However, Shin et al. (2014, Figure 2) focused on fixed energy of 719 keV, and Xiang et al. (2016) and Kim et al. (2016) analyzed only limited periods of time. Neither of them explicitly compared the radial smoothness of the electron flux between lower and higher *L*-shells nor constructed their statistics in the |MLAT|-energy (or *L*-energy) space. Hence, our results complement the previous studies in the following respect: The contrasting latitudinal (or *L*-shell) smoothness of LEO outer-belt electrons between lower and higher *L*-shells is (a) a statistically robust feature identifiable even in year-long averages and (b) valid at least over the energy range between 0.03 and 0.08 MeV covered by MEPD (Figure 1).

Note that the MEPD observations in Figure 1 are relevant to low solar activity, where geomagnetic activity (e.g., frequency of injections) is inherently low. These specific conditions may have further enhanced the spikiness for |MLAT|>66°. Therefore, it would be warranted to extend the MEPD statistics when the data for higher solar activity become available in a few years.

3.3. Correlation With Geosynchronous Electron Flux: GOES-17/MPS-HI

For validating the NextSat-1/MEPD and HEPD data against an independent data set, we adopt observations from geosynchronous satellites. Note that similar inter-comparison was conducted for VAP data by Baker et al. (2019). We use the Geostationary Operational Environmental Satellite 17 (GOES-17) data from the "Space Environment In-Situ Suite" (https://www.ngdc.noaa.gov/stp/satellite/goes-r.html). GOES-17 is one of the satellites in the GOES-R series. We adopt electron flux at 10 different energy channels from the onboard "Magnetospheric Particle Sensors – High" (MPS-HI). Among its 5 telescopes pointing toward different directions, we opt for Telescope 4 directed radially outward (i.e., nearly perpendicular to the background magnetic field). We select the data obtained from January 2020 to February 2021. Only the data between 06–12 h in universal time (UT), which corresponds approximately to local nighttime at the GOES-17 longitudes (LT ∼ UT-9 h), are compared to the nightside (∼2230 LT) NextSat-1/ISSS data.

The data sets for inter-comparison are selected in the following way. The NextSat-1/HEPD and MEPD data at |MLAT| = 66°±2° on the nightside LT are averaged each day. The GOES-17/MPS-HI data between 06 and 12 h in UT are also daily averaged. Then, the NextSat-1 and GOES-17 data on the same date and at nearby energy channels are matched with each other and presented as a point in a scatterplot. Figure 3 presents the scatterplots for a selected energy range from NextSat-1/MEPD-B: 0.06 ± 0.02 MeV. The corresponding energy channel of GOES-17/MPS-HI is 0.065 MeV. The correlation coefficient (*R*) is annotated in the panel. The black dashed lines represent the line of one-to-one correspondence, where the GEO and LEO fluxes are exactly the same. The blue solid line results from the total linear regression method: The slope (0.95) and *y*-intercept (3.11) are also annotated in the figure. Two features in Figure 3 are worth noting. First, the LEO (NextSat-1/MEPD-B) and GEO (GOES-17/MPS-HI) electron fluxes are correlated positively. The correlation coefficient ("*R*" in the figure annotation) is 0.66. Second, the GEO flux is always higher than the LEO flux (intercept ∼ 3, signifying three-order difference), while the slopes of the GEO-LEO scatter points are nearly the same as that of the one-to-one correspondence line (slope = 0.95). That is, when GEO flux increases by an order of magnitude, so does the LEO flux approximately. These two points are consistent with previous studies. For example, Rodger et al. (2010a, Figure 7) reported a positive correlation between GEO and LEO electron flux. Reidy et al. (2021, Figure 3) suggest that GEO flux (equatorially trapped) is larger than LEO flux (near the loss cone). Recently, Pierrard et al. (2021, Figure 10) demonstrated that ∼0.5-MeV electron flux at LEO is 2–3 orders lower than that near the magnetic equatorial plane. This result is in general agreement with the intercept of three in Figure 3, which represents flux level difference of about three orders between the LEO and GEO data.

For the data set shown in Figure 3, we have additionally conducted power-law spectral fit (Whittaker et al., 2013) to electron flux. The daily averaged electron fluxes measured by GOES-17/MPS-HI or NextSat-1/MEPD are fit to the following equation:

$$\log_{10} f = S \times \log_{10} E + A \quad (1)$$

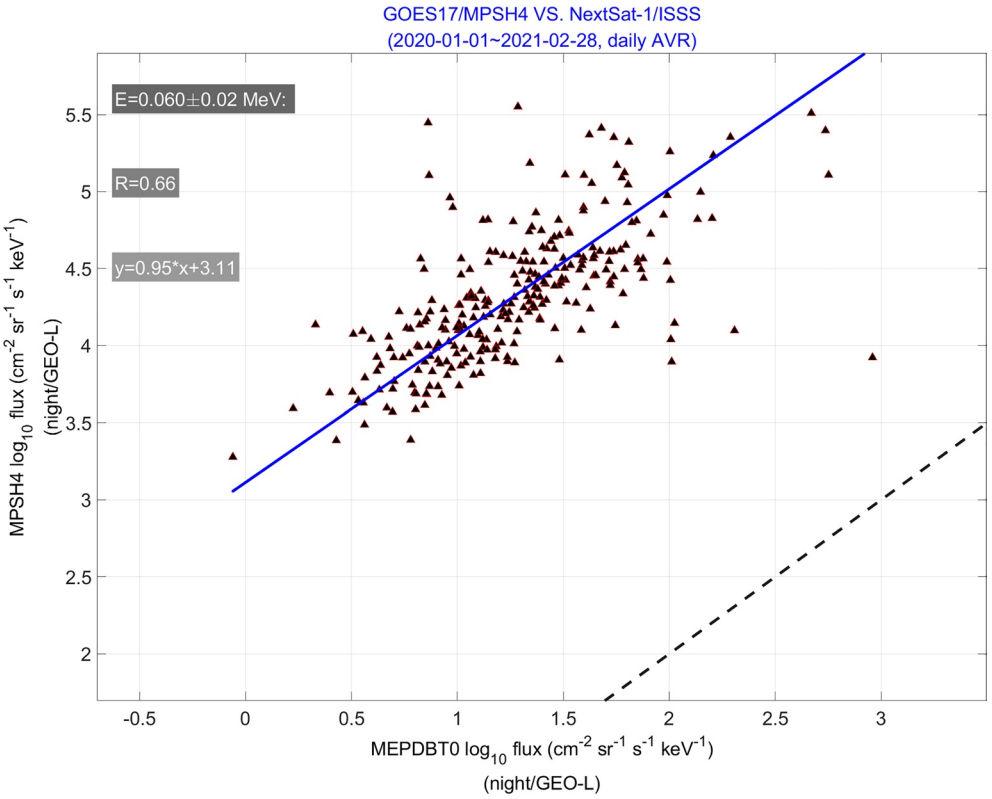

Figure 3. Scatterplots of daily averaged nightside electron flux measured by Next-Generation Small Satellite-1/Medium-Energy Particle Detector-B (abscissa) and Geostationary Operational Environmental Satellite 17/Magnetospheric Particle Sensors - High (ordinate) for 0.06 ± 0.02 MeV. The black dashed lines represent the line of one-to-one correspondence. The blue solid line represents the results of total linear regression. The correlation coefficient (R) and the total regression equation are annotated in the panel.

where f represents the electron flux, E the center energies of instrument energy channels, S the spectral index, and A an offset term. As a result of the fit, we get one spectral index (S) per day per satellite. For GOES-17/MPS-HI, all the 10 energy channels, which have the nominal center energies between 0.065 and 3.3 MeV, are used in the spectral fit. Note that the bowtie center energies can be slightly different from the nominal ones (Boudouridis et al., 2020), but in this study we simply use the nominal values in the "GOES R Series Product Definition and Users' Guide" (Revision 2.2: December 17, 2019). For NextSat-1/MEPD, 12 energy channels between 0.035 and 0.057 MeV are used: Higher energy channels are unused, in order that we can conservatively remove possible effects of high-energy penetrating particles, as will be discussed later in Section 4.2. Examples of the spectral fit are shown in Figure 4: (a) NextSat-1/MEPD-B (DET0), (b) NextSat-1/HEPD (TEL2), and GOES-17/MPS-HI (TEL4). Back in Figure 3, the spectral indices for GOES-17/MPS-HI are statistically −3.38 ± 0.48 (median ± standard deviation) while those of NextSat-1/MEPD are −3.20 ± 1.33. These values agree well with each other.

The spectral indices given above are slightly more negative (i.e., larger in magnitude) than in some previous studies. Using the DEMETER observations in the energy range between 0.07 and 2.34 MeV, Whittaker et al. (2013, Figure 7) reported spectral indices of about −2.5 in the outer belt. According to Chen et al. (2020, Figure 3d), who analyzed data from VAP and a Chinese navigation satellite in the range of the first adiabatic invariant between 1 MeV/G and 10,000 MeV/G, the spectral index (S) near the geosynchronous orbit is about −2. Note that the original spectral indices given in Chen et al. (2020, Figure 3d) are measured in phase space density, which is one less than that measured in differential flux: That is, the former represents $S-1$ in Equation 1 while the latter is S. Also, a review of Oka et al. (2018) states that the spectral index near the geosynchronous orbit is around −2. The reason why both GOES-17 and NextSat-1 report more negative (i.e., softer) spectral indices than in those references is unclear. We speculate that the low solar/geomagnetic

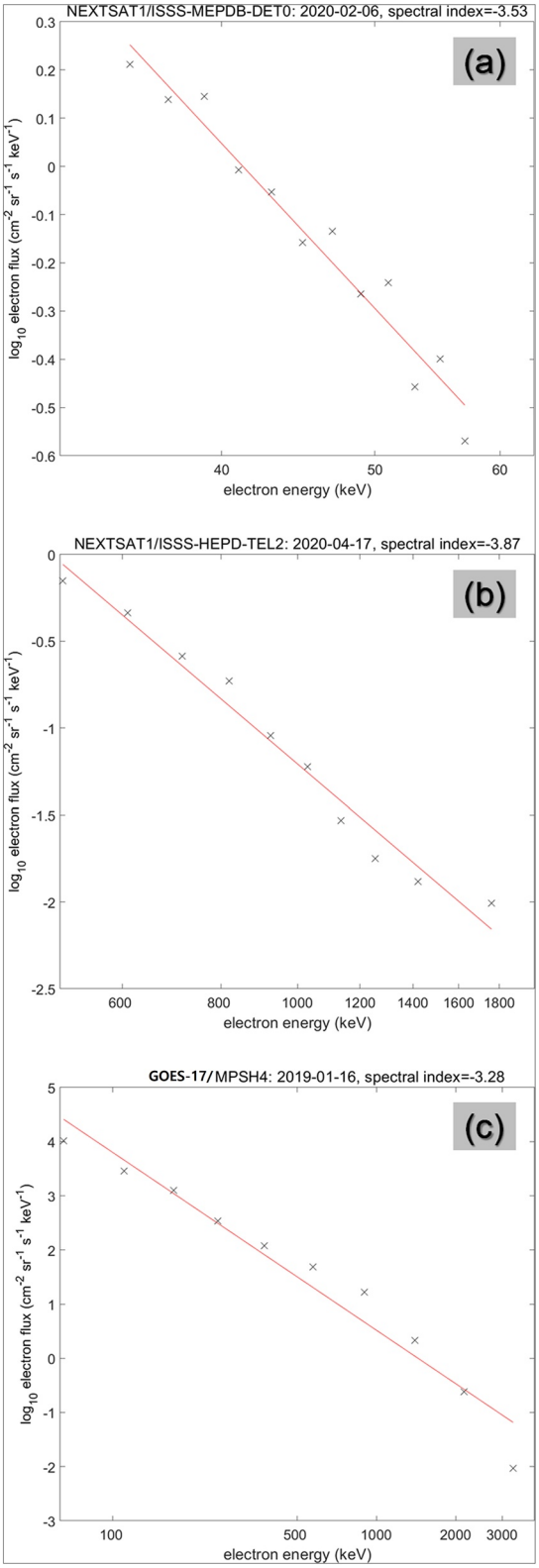

Figure 4. Examples of power spectral fit to the data sets used for correlation analyses between Geostationary Operational Environmental Satellite 17 (GOES-17) and Next-Generation Small Satellite-1 (NextSat-1): (a) NextSat-1/Medium-Energy Particle Detector-B (DET0), (b) NextSat-1/High-Energy Particle Detector (TEL2), and (c) GOES-17/Magnetospheric Particle Sensors - High (TEL4).

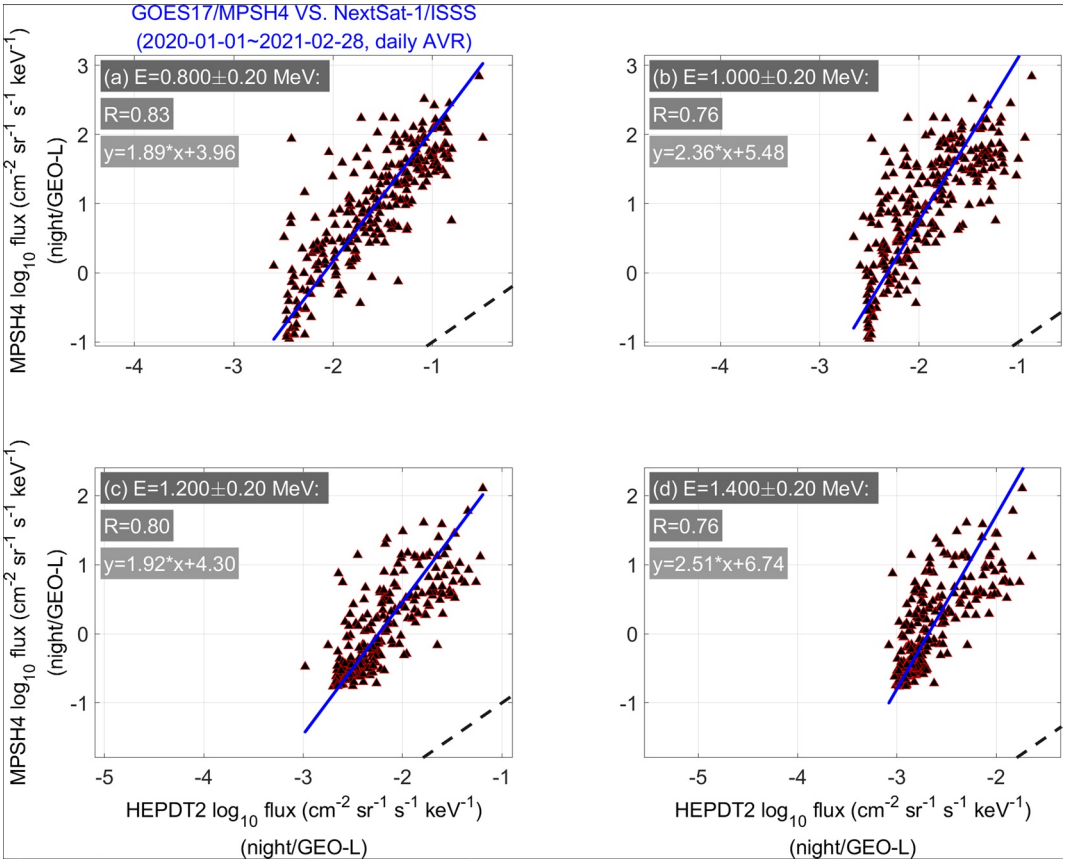

Figure 5. Similar to Figure 3, but based on Next-Generation Small Satellite-1/High-Energy Particle Detector-T2 data for the abscissa representing higher energy channels.

activity during our analysis period (around 2020) may partly explain it. According to Miyoshi et al. (2003, Figure 9), Meredith et al. (2002), Oka et al. (2018), and Park et al. (2018), spectral hardening occurs during the long-lasting recovery of storms. Therefore, overall weak geomagnetic activity around the solar-minimum year 2020 may be one of the reasons for the softer (more negative) spectral indices in our study. Note, however, that Zhao et al. (2019a, Figure 7c) reported power spectral indices (in the energy range between 100 keV and 10 MeV) for $L > 6$ being generally much softer than −2. Also, van de Kamp et al (2018) statistically demonstrated that spectral indices calculated from POES observations (in the energy range between 0.03 and 1 MeV) are around −3.5. These two papers support the spectral indices we estimated from NextSat-1 and GOES-17. The conflicting results among different studies may also originate from the fact that energy spectra of radiation belt electrons are not strictly power-law (e.g., Zhao et al., 2019a). In addition, different spatial and energy ranges used in different studies can contribute to the discrepancy, which suggests that more observational data need to be accumulated to elucidate the spectral shapes for radiation belt electrons.

Figure 5 is similar to Figure 3, but for higher energy ranges measured by NextSat-1/HEPD-T2. The reference energy channels of GOES-17/MPS-HI are 0.9 MeV for panels a and b and 1.4 MeV for panels c and d. The two points discussed above as to Figure 3 (i.e., positive correlation and magnitude difference between the LEO and GEO electron flux) generally remain valid for Figure 5: The GEO-LEO correlation coefficients are slightly higher for the latter (HEPD: higher energies) than for the former (MEPD: lower energies). On the other hand, the total linear regression results (the blue solid line and equation in each panel) are different from those in Figure 3: The slope is significantly larger than unity, and the y-intercept is much larger than in Figure 3. We will come back to these issues in Section 4.

For the data set shown in Figure 5, we also conduct spectral fit as was done for Figure 3. Ten energy channels of NextSat-1/HEPD between 0.5 to 1.76 MeV are used for the fit, as shown in Figure 4b. The results for GOES-17/MPS-HI are -3.42 ± 0.46 (median $\pm$ standard deviation), and those of NextSat-1/HEPD are -3.18 ± 1.01. Note that the GOES-17/MPS-HI result for Figure 5 is not exactly the same as for Figure 3 because the GOES-17 data used are slightly different according to the different availability of coincident NextSat-1 (MEPD or HEPD) data. In summary, (a) the high correlation between NextSat-1 and GOES-17 electron flux and (b) their spectral index ranges similar to each other support the reliability of both data sets.

The GEO-LEO correlation coefficients are generally lower in Figure 3 (lower energies) than in Figure 5 (higher energies). This may be put in the context of VAP observations reported previously. Reeves et al. (2016, Figures 2, 7, and 8) demonstrated that lower-energy electrons in the outer radiation belt exhibit larger spatio-temporal variations than higher-energy electrons. The GEO data points in Figures 3 and 5 correspond to the same dates as those of LEO data. To obtain reasonably good data coverage, however, we average the LEO data over a range of |MLAT| values (i.e., including those not exactly corresponding to the GEO footprints). What is more, the NextSat-1/ISSS does not operate continuously over the course of a day, but only for several passes selected by ever-changing operation scenarios. GOES-17/MPS-HI data are similarly averaged over a 6-hour UT (equivalently, LT) range to guarantee sufficient data coverage. If low-energy electrons exhibit strong spatio-temporal variability as reported by Reeves et al. (2016), the spatio-temporal averaging scheme of the NextSat-1 (LEO) and the GOES-17 (GEO) data can lower the correlation coefficients of the low-energy electrons.

4. Discussions

4.1. Miscellaneous Features in the NextSat-1 Data

In addition to the main findings presented in Section 3, some other aspects in Figures 1 and 2 are worth further discussion. This subsection is devoted to those additional features.

First, Figure 2 demonstrates that inner-belt (|MLAT|<55°) electrons generally have energies around 0.505 MeV for both quiet and disturbed periods of years 2019–2021. This is consistent with the VAP observations during Solar Cycle 24, which showed that MeV electrons in the inner belt are rarely found or only have weak flux levels (e.g., Fennell et al., 2015; Ripoll et al., 2016; Claudepierre et al., 2019).

Second, Figure 2 shows that locally precipitating electrons (inside the loss cone; Figures 2a and 2b) are slightly biased toward higher |MLAT| than the locally trapped population (near the loss cone edge; Figures 2e and 2f) for all energy channels. This result agrees with Rodger et al. (2010a, Figure 5) based on data from the Space Environment Monitor onboard the POES satellite. In that paper, the ratio of locally trapped to precipitating electrons at >0.7 MeV is much higher for $L < 6.6$ (approximately |MLAT|<66° in our Figures 1 and 2) than for $L > 6.6$. In summary, all the features discussed in this subsection agree well with previous studies, supporting the reliability of the NextSat-1 data sets.

4.2. MEPD and HEPD Data Quality

This subsection presents a few known caveats to the NextSat-1/MEPD and HEPD data. Information given here may be used as a guide for future users of NextSat-1/ISSS.

4.2.1. MEPD Data Quality

For electron energies larger than ~0.08 MeV, which is not shown in Figure 1, MEPD spectra exhibit unexpected flattening or rising. Figure 6d, reproduction of Figure 1c but over a wide energy range, exemplifies this feature: see the red horizontal arrow. A plausible reason for the artifacts is high-energy electrons penetrating the MEPD Silicon detector, as described schematically in Figures 6a–6c. For the electrons fully stopped inside the Silicon detector (Figure 6a), the deposited energy is the same as the incident energy we want to measure. On the contrary, higher-energy electrons which penetrate through the detector (Figure 6b) deposit there only a part of the incident energy. For Silicon detectors, the relationship between the incident and deposited electron energy generally has a non-monotonic shape, as pictorially described in Figure 6c. Hence, even if an energy spectrum of incident electrons is monotonic (see the number of small green circles

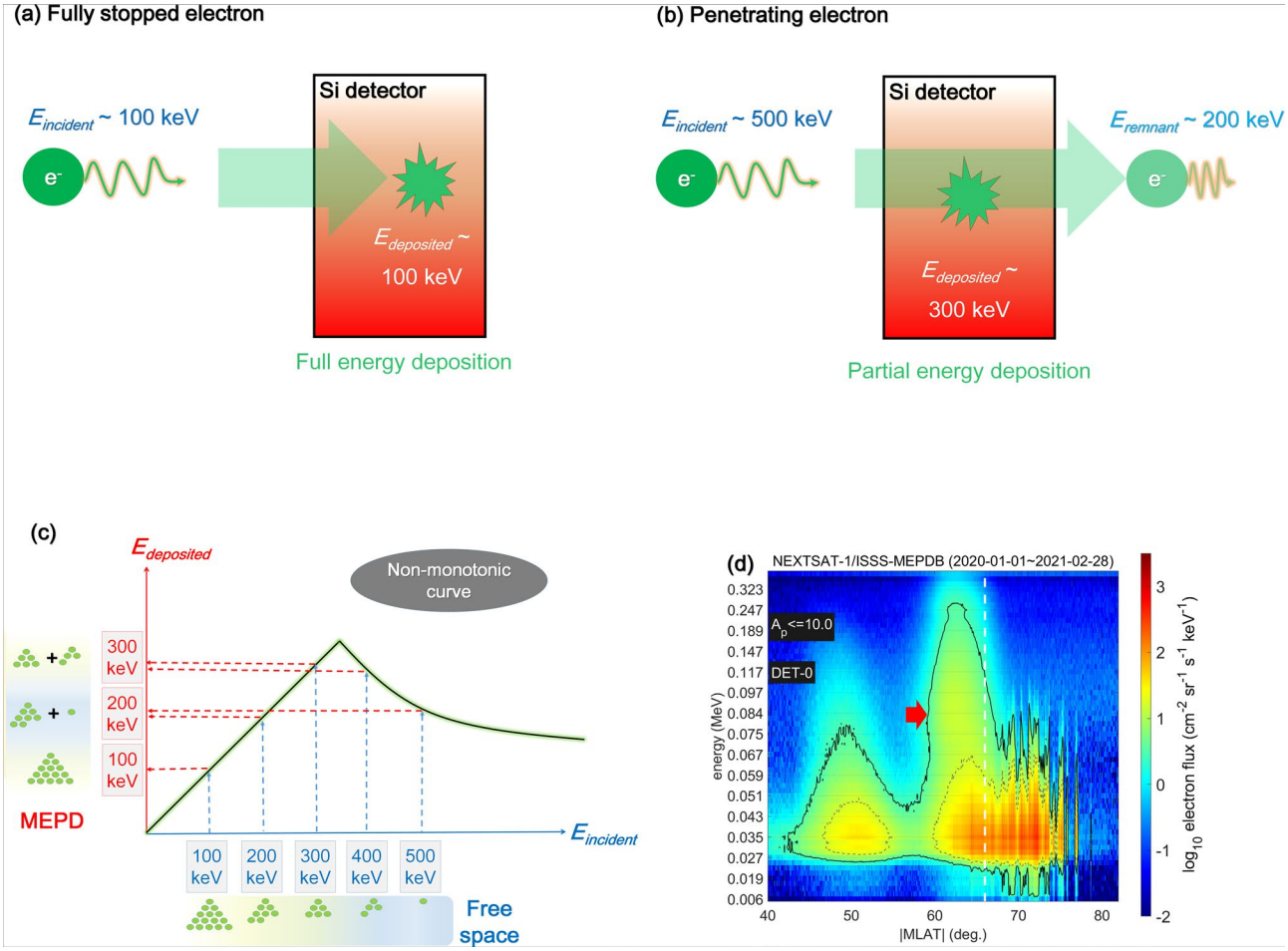

Figure 6. Schematic diagrams describing full and partial deposition of electron energies onto the Next-Generation Small Satellite-1 (NextSat-1)/Medium-Energy Particle Detector (MEPD). (a) Full energy deposition of an electron stopped by the Silicon detector, (b) partial energy deposition of an electron penetrating the detector, and (c) relationship between the incident (abscissa) and deposited (ordinate) energies of electrons. For each energy channel in panel c, the number of small green circles represents the number of electrons having the incident (abscissa) or deposited (ordinate) energy. Panel d exemplifies non-monotonic dependence of electron flux on energy in the NextSat-1/MEPD data, which is annotated with a red horizontal arrow.

below the abscissa), the deposited energy spectra may not (see the green circles around the ordinate). This artifact might have been suppressed if the MEPD had an additional Silicon detector on the rear side, which can signal whether an electron has penetrated the front detector or not. Unfortunately, the MEPD only has a front Silicon detector with a thickness of ~315 μm, whose energy limit for full electron stop is about 225 keV (Seo et al., 2021). This inherent limitation might have created the slightly non-monotonic energy spectrum in Figure 6d. To alleviate this issue, we have only used a part of the energy channels for spectral analyses of NextSat-1/MEPD, as described in Section 3. Further efforts are called for to remove this artifact. However, this limitation does not severely compromise our main conclusion, and its correction is left for future works.

Another feature notable in the MEPD data is the relative flux levels of MEPD-A (precipitating electrons) and MEPD-B (locally trapped population) in Figure 1. In the outer radiation belt, the former looks stronger than the latter (see Figures 1e and 1f), which does not agree with a number of previous papers based on POES satellites. Those papers reported that the POES 90° telescopes (corresponding to NextSat-1/MEPD-B) generally record electron fluxes higher than the POES 0° telescopes (corresponding to NextSat-1/MEPD-A): see, for example, Rodger et al. (2010a, Figure 5) and Søraas et al. (2018, Figure 4).

We note the wide FOV of NextSat-1/MEPD: Its half-width in the pitch angle direction is ~35°, which is more than double that of NOAA-POES (~15°). Due to their wide FOVs, MEPD-A and MEPD-B do not cover so drastically different pitch angle ranges as POES 0° and 90° telescopes do. We expect that pitch-angle

anisotropy in the NextSat-1/MEPD data be weaker than for NOAA-POES, but we still need to explain why the precipitating electrons look more abundant than the trapped ones.

By design, the signal discriminator of MEPD-A and MEPD-B, which discriminates small noise from valid event signals, share the same reference voltage assigned by the onboard computer. However, by investigating the in-orbit electron energy spectra, we have found that the same reference voltage (e.g., 160 mV) results in different threshold energies for MEPD-A (~12 keV) and MEPD-B (~26 keV). Therefore, MEPD-B (locally trapped) electrons should overcome the higher energy threshold to be registered as a valid event, and this may contribute to the flux reduction to some degree. This instrument configuration is difficult to be improved because NextSat-1 cannot give two different reference voltages (related to threshold energies) to MEPD-A and MEPD-B.

Overall, the pitch angle distribution in the MEPD-A and MEPD-B data remains an issue to be resolved, and users are advised not to quantitatively compare the MEPD-A and MEPD-B. Still, the Ap-dependent slot region locations in agreement with previous studies (Figure 1) and the good correlation with the GOES-17 data (Figure 3) support that MEPD data can be qualitatively used for radiation belt monitoring. Efforts to resolve this pitch angle issue are currently ongoing, and will be considered for later versions of the MEPD data.

4.2.2. HEPD Data Quality

As for HEPD, the scatterplots in Figure 5 exhibit a droop-down trend for low-flux ranges. That is, the GEO-LEO correlation worsens in these low-flux regimes, and the LEO flux seems to be over-estimated. This trend implies that NextSat-1/HEPD data may be affected by artificial noise, whose relative effect becomes more significant for regions where natural electron flux is lower. As can be seen in Figures 2e and 2f, NextSat-1/HEPD-T2 data exhibit blurry, horizontal (i.e., constant-energy) stripes around 0.8 MeV over a wide |MLAT| range in the spectrograms. The stripes are suspected to result from electronics noise. As a result, when natural electron flux within the measurable energy range is low at both GOES-17 and NextSat-1 locations, the noise of the NextSat-1/HEPD can lead to a large amount of mistakenly recorded electron counts. The noise can also blur weak, if any, signals of >0.505 MeV in the inner belt (e.g., Claudepierre et al., 2019). Hence, the absolute level of the NextSat-1/HEPD flux, especially when the overall flux levels are low, should be interpreted with caution.

This noise effect (i.e., the droop-down trend in Figure 5) must have contributed to the slope and *y*-intercept in Figure 5, both of which are unexpectedly larger than for the NextSat-1/MEPD data (Figure 3). The droop-down trend in the low-flux regime in Figure 5 can lead to large slope and *y*-intercept in the correlation diagrams. Therefore, we expect that the slope and *y*-intercept in Figure 5 (NextSat-1/HEPD) would be similar to those in Figure 3 (NextSat-1/MEPD) if the HEPD noise effects were cleaned up by some advanced methods.

4.3. Ethnology of the "Locally Trapped" Electrons

It is well known that "locally trapped" electrons at LEO do not necessarily correspond to "stably trapped" populations (e.g., Yang et al., 2017, Figure 1). Due to the existence of the SAA, where magnetic field intensity decreases significantly, some of the locally trapped electrons can be lost once they reach the SAA during zonal drift motion. This population is termed quasi-trapped electrons or electrons in the "drift loss cone" (DLC). Furthermore, a part of the locally trapped electrons, if they are at the northern conjugate region to the SAA, can be lost within one bounce motion: They are called untrapped electrons or electrons in the "bounce loss cone" (BLC). It is worth discussing how much of the locally trapped electrons observed by NextSat-1/ISSS can be categorized into each of the three populations: BLC, DLC, and stably trapped electrons. The discussions can be helpful information to future users of NextSat-1/ISSS.

Figure 7 presents the composition map of the locally trapped electrons measured by NextSat-1/ISSS. To draw this figure, we first calculate the magnetic field strength both at the nominal altitude of NextSat-1 (575 km) and at 110 km height, using the CHAOS magnetic field model (https://www.space.dtu.dk/english/research/scientific_data_and_models/magnetic_field_models). For each grid point at 575 km height (1-by-1 degree in geographic longitude and latitude), we compare the local magnetic field strength (B_{575})

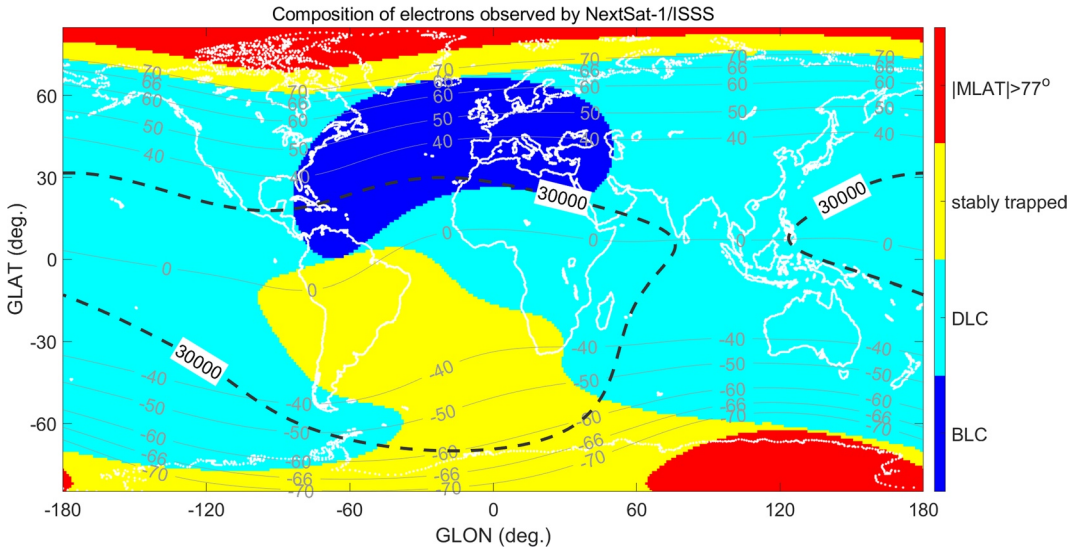

Figure 7. Global map showing the composition of locally trapped electrons detected by Next-Generation Small Satellite-1 (NextSat-1)/Instrument for the Study of Space Storms: bounce loss cone (deep blue), drift loss cone (light blue), stably trapped (yellow), and magnetic latitude (|MLAT|) > 77° (red) electrons. The gray contour lines with text annotations represent quasi-dipole latitudes calculated for the nominal altitude of NextSat-1 (575 km). The thick black dashed curve signifies magnetic field strength of 30,000 nT at the NextSat-1 altitude as calculated by the CHAOS model.

and those of the conjugate points at 110 km height ($B_{\text{conjugate-110}}$). The conjugate points and the original grid point share the same |Apex latitude| (equivalent to the L-shell) and magnetic longitude, as defined by Laundal and Richmond (2017). If the B_{575} is larger than $B_{\text{conjugate-110}}$, the original grid point at the 575 km height is considered as the BLC (untrapped) population. Next, assuming that electrons drift zonally along contours of constant L-shell (practically equivalent to constant |Apex latitude|), we also compare the B_{575} with those at 110 km having the same |Apex latitude| and different magnetic longitudes ($B_{\text{same-Apex-110}}$). If the B_{575} is smaller than $B_{\text{conjugate-110}}$ but larger than any of the $B_{\text{same-Apex-110}}$ values along the electron drift path, the original grid point at 575 km height is considered as the DLC (quasi-trapped) population. Locations at |MLAT|>77° are neglected because magnetic field lines there are likely to be open (i.e., conjugate points are undefined). All the other regions at 575 km height are deemed to represent "stably trapped" electrons. After all these procedures, the resultant world map is filtered with a 2-dimensional median filter (5-by-5 points) to smooth out interpolation errors.

The color palette in Figure 7 represents the electron composition: BLC (deep blue), DLC (light blue), stably trapped electrons (yellow), and regions at |MLAT|>77° (red). The gray solid contour lines with numbers correspond to quasi-dipole latitudes (e.g., Laundal and Richmond, 2017) at the nominal altitude of NextSat-1 (575 km). The thick black dashed curve signifies magnetic field strength of 30,000 nT at the nominal NextSat-1 altitude of 575 km (calculated from the CHAOS model), which roughly corresponds to the SAA region inside which we discarded NextSat-1/ISSS data.

Figure 7 is in good agreement with previous studies, such as Rodger et al. (2010b, Figure A2), Yang et al. (2017, Figure 1), and Greeley et al. (2019, Figure 1). At regions of |MLAT|<66° (i.e., equatorward of the GEO footprint), locally trapped electrons (e.g., MEPD-B and HEPD-T2) are mainly composed of BLC (deep blue) and DLC populations (light blue), both of which are eventually lost within one drift period. Note that HEPD electrons (with energies >0.4 MeV) almost exclusively reside in these regions (|MLAT|<66°). On the other hand, at locations of |MLAT|>70°, which still accommodate some of the MEPD electrons in Figure 1, a significant part of the locally trapped population is "stably" trapped. In summary, the locally trapped electrons observed by NextSat-1/ISSS generally belong to BLC and DLC particles close to the edge of the loss cone (especially for energies >0.4 MeV; HEPD). On the contrary, contributions of stably trapped electrons become non-negligible for |MLAT|>70°, where structured electrons at lower energy (MEPD) are detected: see Figure 1.

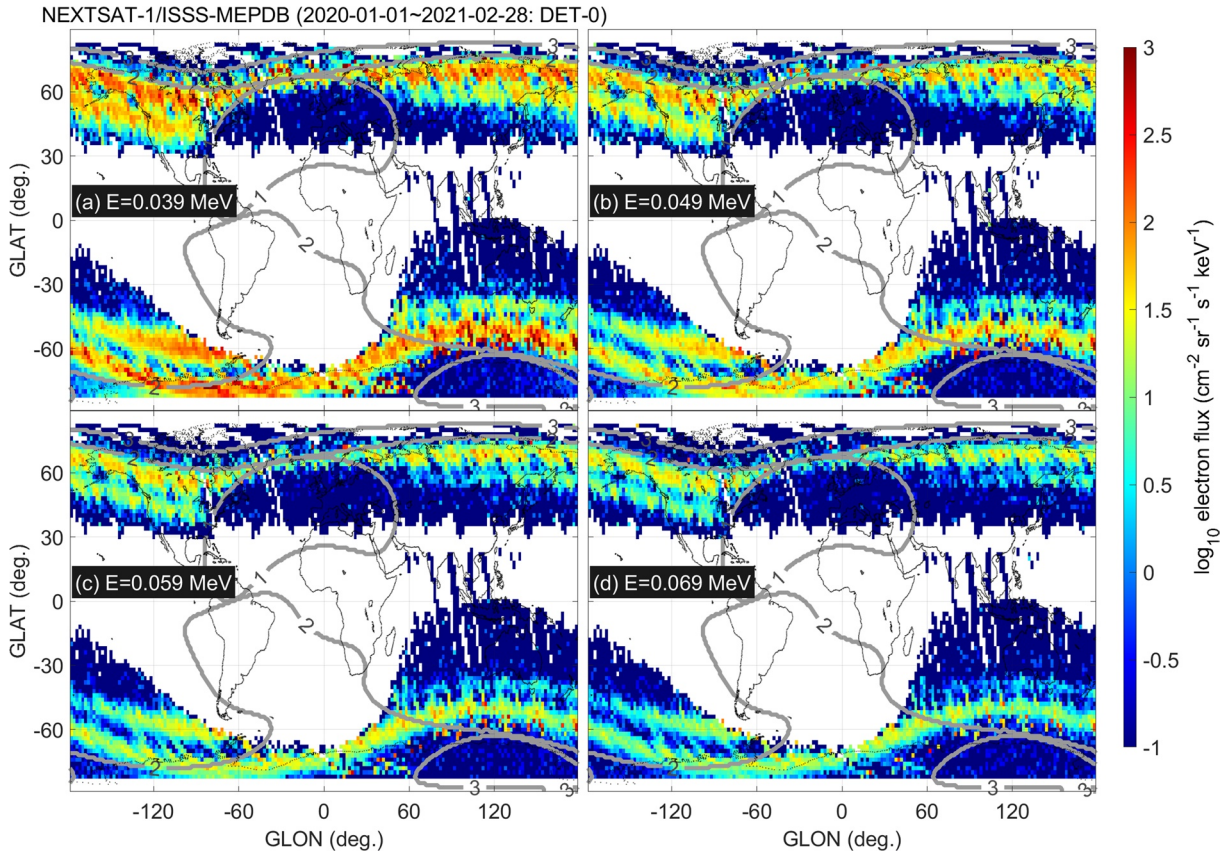

Figure 8. Global map of locally trapped electron flux as measured by Next-Generation Small Satellite-1/Medium-Energy Particle Detector. Each panel represents an energy channel. Two-belt structures are clearly identified in each panel. The gray contour lines correspond to the composition of locally trapped electrons as described in Figure 7.

Figure 8 presents global maps of locally trapped electron flux observed by MEPD. Figure 9 is similar to Figure 8, but for HEPD. Each panel represents a different energy channel. The gray contour lines correspond to the categorization given in Figure 7 (<1: bounce loss cone, 1∼2: drift loss cone, 2∼3: stable trapping, >3: |MLAT|>70°). Note that the South Atlantic regions are largely void of colored pixels because we discard NextSat-1 data if the observed |B| is smaller than 30,000 nT, by which we can minimize ion-to-electron contamination by the SAA.

Both Figures 8 and 9 agree with expectations from Figure 7 and also with previous studies, such as Whittaker et al. (2014, Figure 2), in the following respects. First, the inner belt (more equatorward band) is very weak to the immediate east of the Atlantic longitude sector, but the intensity gradually increases toward east: This feature is common for both hemispheres. It is because locally trapped electrons in the inner belt outside the SAA are eventually removed in the SAA after their eastward drift: see Figure 7. Second, for the outer belt (more poleward band), the longitude dependence of electron flux is relatively weak. The outer belt near the Northern Atlantic Ocean appears slightly weaker than in the other longitude regions, which is consistent with the expectations from Figure 7. The locally trapped electrons in that region are lost within one bounce period. Such behavior can also be seen in Suvorova (2017, Figure 1) based on the POES data. Third, the HEPD electrons (Figure 9) clearly show the inner band for 0.505 MeV (panel a) while the structure gets vague as the electron energy increases. This is again consistent with recent Van Allen Probes studies, which reported the rarity of MeV electrons in the inner belt during Solar Cycle 24 (e.g., Fennell et al., 2015). The good agreement between Figures 8 and 9 and previous studies further supports the reliability of the data quality of NextSat-1/MEPD and HEPD.

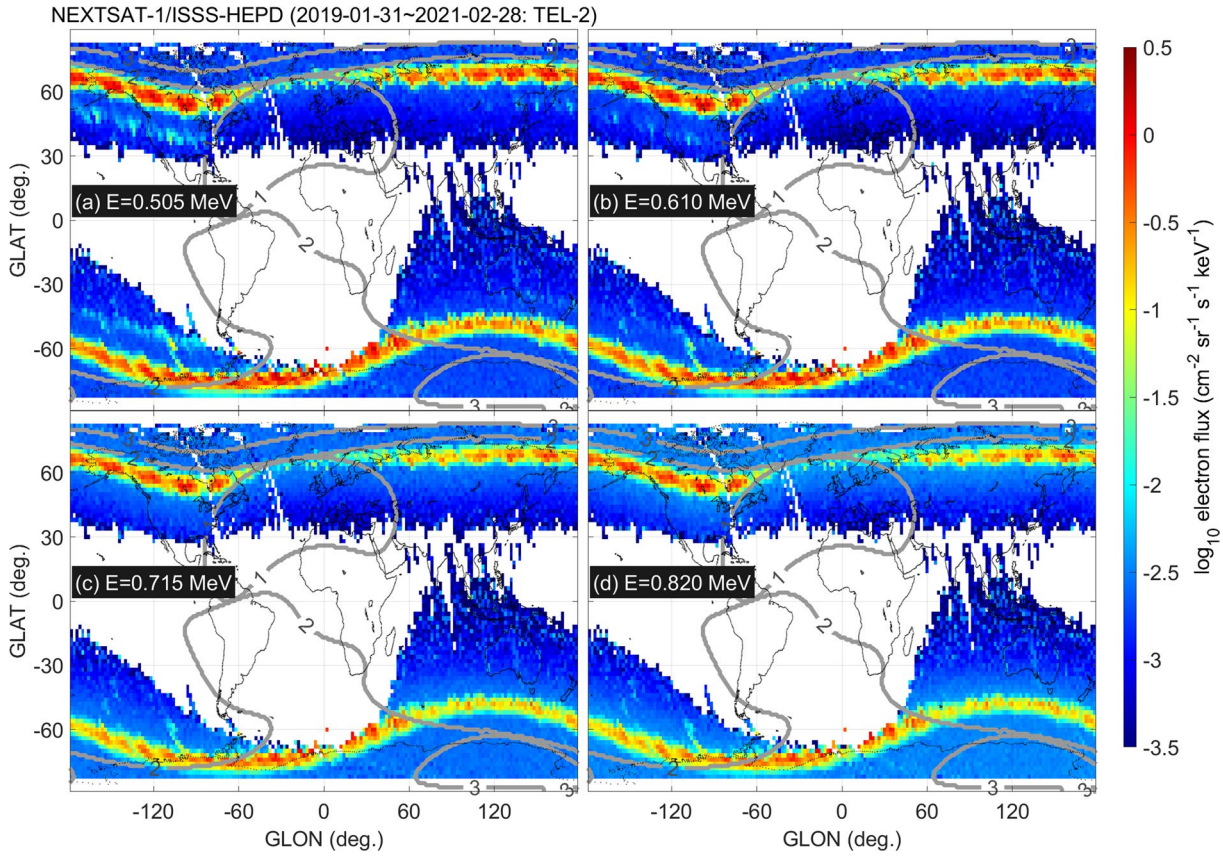

Figure 9. Similar to Figure 8, but for Next-Generation Small Satellite-1/High-Energy Particle Detector.

5. Summary and Conclusions

Energetic electron observations at LEO by NextSat-1 are statistically analyzed in this paper. Though similar studies have been conducted earlier at other orbits, our results reveal a number of features that were not explicitly addressed by previous papers and remained as a niche market. The main findings of NextSat-1 are summarized as follows:

1. [*Slot region*] For <1 MeV electrons, the slot region behavior in the |MLAT|-energy space agrees with VAP observations near the equatorial plane: injection of low-energy electrons for increasing geomagnetic activity.
2. [*Inside* versus *outside the GEO footprints*] The |MLAT| profiles of 30–80 keV electron flux are generally smoother equatorward of the GEO footprints than poleward, irrespective of energy channels and geomagnetic activities.
3. [*LEO-GEO correlation*] Daily averaged nightside electron fluxes of NextSat-1 (LEO) and GOES-17 (GEO) at nearby *L*-shells and MLTs are positively correlated, with the coefficients generally higher for the higher electron energy range. The LEO flux is lower than the GEO flux, but the slope between their logarithms is about 1–2.5.
4. [*LEO-GEO spectral indices*] Daily averaged nightside electron fluxes of NextSat-1 (LEO) and GOES-17 (GEO) at nearby *L*-shells have similar spectral index ranges, around −3. This spectral index is slightly softer (more negative) than in some previous studies, such as Whittaker et al. (2013) and Chen et al. (2020), while being in good agreement with van de Kamp et al. (2018).

Overall, the NextSat-1 observations climatologically depict how energetic electrons at LEO change with energies, pitch angles, and geomagnetic activities. Note that the data used in this study are mostly limited to a pre-midnight sector (2230 LT) during solar-minimum years (2019–2021). The China Seismo-Electromagnetic Satellite (CSES), which was also launched in 2018, has been measuring fine energy spectra of LEO

electrons at post-midnight regions (0200 LT). Inter-comparison between NextSat-1 and CSES electron fluxes may reveal whether the conclusions obtained by NextSat-1 remain valid in the post-midnight sector, which will be an interesting topic for a follow-up study.

As of June 2021, NextSat-1/ISSS conducts observations for 6 passes per day on average. All the quicklook plots are open to the public with a latency of 5 working days, and the HEPD and MEPD data in the Hierarchical Data Format (HDF) are provided at the official web page for registered users. Together with other missions in this post-VAP era, the NextSat-1/ISSS can contribute useful information on the radiation belt to the space science community. In addition to the particle and cold plasma observations described above, magnetic field data from the onboard FGM are being calibrated by empirical geomagnetic field models, following Olsen et al. (2020) and Stolle et al. (2021). As soon as the calibration is finished, the magnetic field data will also be made available to the public.

Data Availability Statement

The NextSat-1/ISSS quicklook plots are available at http://n1isss.kaist.ac.kr/03_01.php: users can select from the tab the year and month of interest (e.g., 202011 for November 2020). The HDF data files are available, after registration, at: http://n1isss.kaist.ac.kr/bbs/login.php?url=%2F03_01.php. GOES-17 data are open to the public at https://data.ngdc.noaa.gov/platforms/solar-space-observing-satellites/goes/.

Acknowledgment
The authors gratefully thank all the engineers at the Satellite Technology Research Center of Korea Advanced Institute of Science and Technology for their effort in NextSat-1 operations. Jaeheung Park was supported by the KASI project, 'Research on next-generation space weather variation and prediction.'

References

Baker, D. N., Zhao, H., Li, X., Kanekal, S. G., Jaynes, A. N., Kress, B. T., et al. (2019). Comparison of Van Allen Probes energetic electron data with corresponding GOES-15 measurements: 2012–2018. *Journal of Geophysical Research: Space Physics*, *124*, 9924–9942. https://doi.org/10.1029/2019JA027331

Blum, L., Li, X., & Denton, M. (2015). Rapid MeV electron precipitation as observed by SAMPEX/HILT during high-speed stream-driven storms. *Journal of Geophysical Research: Space Physics*, *120*, 3783–3794. https://doi.org/10.1002/2014JA020633

Boudouridis, A., Rodriguez, J. V., Kress, B. T., Dichter, B. K., & Onsager, T. G. (2020). Development of a bowtie inversion technique for real-time processing of the GOES-16/-17 SEISS MPS-HI electron channels. *Space Weather*, *18*, e2019SW002403. https://doi.org/10.1029/2019SW002403

Boyd, A. J., Turner, D. L., Reeves, G. D., Spence, H. E., Baker, D. N., & Blake, J. B. (2018). What causes radiation belt enhancements: A survey of the Van Allen Probes Era. *Geophysical Research Letters*, *45*, 5253–5259. https://doi.org/10.1029/2018GL077699

Capannolo, L., Li, W., Spence, H., Johnson, A. T., Shumko, M., Sample, J., & Klumpar, D. (2021). Energetic electron precipitation observed by FIREBIRD-II potentially driven by EMIC waves: Location, extent, and energy range from a multievent analysis. *Geophysical Research Letters*, *48*, e2020GL091564. https://doi.org/10.1029/2020GL091564

Chen, X., Zong, Q., Zou, H., Wang, Y., Zhou, X., & Bernard Blake, J. (2020). Distribution of energetic electrons in the near earth space: New observations from the BeiDa Imaging Electron Spectrometer and the Van Allen Probes. *Planetary and Space Science*, *186*, 104919 ISSN 0032-0633. https://doi.org/10.1016/j.pss.2020.104919

Choi, C. R., Sohn, J., Lee, J.-C., Seo, Y. M., Kang, S.-B., Ham, J., et al. (2014). Scientific missions and technologies of the ISSS on board the NEXTSat-1. *Journal of Astronomy and Space Sciences*, *31*(1), 73–81. https://doi.org/10.5140/jass.2014.31.1.73

Choi, H.-S., Lee, J., Cho, K.-S., Kwak, Y.-S., Cho, I.-H., Park, Y.-D., et al. (2011). Analysis of GEO spacecraft anomalies: Space weather relationships. *Space Weather*, *9*, S06001. https://doi.org/10.1029/2010SW000597

Claudepierre, S. G., O'Brien, T. P., Looper, M. D., Blake, J. B., Fennell, J. F., Roeder, J. L., et al. (2019). A revised look at relativistic electrons in the Earth's inner radiation zone and slot region. *Journal of Geophysical Research: Space Physics*, *124*, 934–951. https://doi.org/10.1029/2018JA026349

De Michelis, P., Consolini, G., Pignalberi, A., Tozzi, R., Coco, I., Giannattasio, F., et al. (2021). Looking for a proxy of the ionospheric turbulence with Swarm data. *Scientific Reports*, *11*, 6183. https://doi.org/10.1038/s41598-021-84985-1

Fennell, J. F., Claudepierre, S. G., Blake, J. B., O'Brien, T. P., Clemmons, J. H., Baker, D. N., et al. (2015). Van Allen Probes show that the inner radiation zone contains no MeV electrons: ECT/MagEIS data. *Geophysical Research Letters*, *42*, 1283–1289. https://doi.org/10.1002/2014GL062874

Greeley, A. D., Kanekal, S. G., Baker, D. N., Klecker, B., & Schiller, Q. (2019). Quantifying the contribution of microbursts to global electron loss in the radiation belts. *Journal of Geophysical Research: Space Physics*, *124*, 1111–1124. https://doi.org/10.1029/2018JA026368

Jeong, W.-S., Park, S.-J., Park, K., Lee, D.-H., Pyo, J., Moon, B., et al. (2014). Conceptual design of the NISS onboard NEXTSat-1. *Journal of Astronomy and Space Sciences*, *31*, 83–90. https://doi.org/10.5140/JASS.2014.31.1.83

Kessel, R. L., Fox, N. J., & Weiss, M. (2013). The radiation belt storm probes (RBSP) and space weather. *Space Science Reviews*, *179*(1-4), 531–543. https://doi.org/10.1007/s11214-012-9953-6

Khazanov, G. V., Liemohn, M. W., Newman, T. S., Fok, M.-C., & Ridley, A. J. (2004). Magnetospheric convection electric field dynamics andstormtime particle energization: Case study of the magneticstorm of 4 May 1998. *Annales Geophysicae*, *22*, 497–510. https://doi.org/10.5194/angeo-22-497-2004

Kim, E., Yoo, J.-H., Kim, H.-E., Seo, H., Ryu, K., Sohn, J., et al. (2020). Initial operation and preliminary results of the instrument for the study of stable/storm-time space (ISSS) on board the next generation small satellite-1 (NEXTSat-1). *Journal of Astronomy and Space Sciences*, *37*(3), 209–218. https://doi.org/10.5140/JASS.2020.37.3.209

Kim, K.-C., Shprits, Y. Y., & Blake, J. B. (2016). Fast injection of the relativistic electrons into the inner zone and the formation of the split-zone structure during the Bastille Day storm in July 2000. *Journal of Geophysical Reasearch: Space Physics*, *121*, 8329–8342. https://doi.org/10.1002/2015JA022072

Laundal, K. M., & Richmond, A. D. (2017). Magnetic coordinate systems. *Space Science Reviews*, *206*, 27–59. https://doi.org/10.1007/s11214-016-0275-y

Lee, C. N., Min, K. W., Lee, J.-J., Hwang, J. A., Park, J., Edelstein, J., & Han, W. (2011). FUV spectrum in the polar region during slightly disturbed geomagnetic conditions. *Journal of Geophysical Research*, *116*, A10319. https://doi.org/10.1029/2011JA016898

Lee, J., Min, K., Ryu, K., Kang, K.-I., Shin, G.-H., Sohn, J., & Na, G. (2018). Space plasma detectors on NEXTSat-1 for ionospheric measurements. *Journal of the Korean Physical Society*, *72*, 1393–1401. https://doi.org/10.3938/jkps.72.1393

Lee, J.-J., Parks, G., Min, K., Hwang, J., McCarthy, M., Lee, E., et al. (2005). Energy spectra of ~170–360 keV electron microbursts measured by the Korean STSAT-1. *Geophysical Research Letters*, *32*, L13106. https://doi.org/10.1029/2005GL022996

Li, W., Thorne, R. M., Nishimura, Y., Bortnik, J., Angelopoulos, V., McFadden, J. P., et al. (2010). THEMIS analysis of observed equatorial electron distributions responsible for the chorus excitation. *Journal of Geophysical Research*, *115*, A00F11. https://doi.org/10.1029/2009JA014845

Li, X., Schiller, Q., Blum, L., Califf, S., Zhao, H., Tu, W., et al. (2013). First results from CSSWE CubeSat: Characteristics of relativistic electrons in the near-Earth environment during the October 2012 magnetic storms. *Journal of Geophysical Research: Space Physics*, *118*, 6489–6499. https://doi.org/10.1002/2013JA019342

Lühr, H., & Xiong, C. (2010). IRI-2007 model overestimates electron density during the 23/24 solar minimum. *Geophysical Research Letters*, *37*, L23101. https://doi.org/10.1029/2010GL045430

Mauk, B. H., Fox, N. J., Kanekal, S. G., Kessel, R. L., Sibeck, D. G., & Ukhorskiy, A. (2012). Science objectives and rationale for the radiation belt storm probes mission. *Space Science Reviews*, *179*, 3–27. https://doi.org/10.1007/s11214-012-9908-y

Meredith, N. P., Horne, R. B., Summers, D., Thorne, R. M., Iles, R. H. A., et. al. (2002). Evidence for acceleration of outer zone electrons to relativistic energies by whistler mode chorus. *Annales Geophysicae*, *20*(7), 967–979. https://doi.org/10.5194/angeo-20-967-2002

Miyoshi, Y., Morioka, A., Obara, T., Misawa, H., Nagai, T., & Kasahara, Y. (2003). Rebuilding process of the outer radiation belt during the 3 November 1993 magnetic storm: NOAA and Exos-D observations. *Journal of Geophysical Research*, *108*(A1), 1004. https://doi.org/10.1029/2001JA007542

Oka, M., Birn, J., Battaglia, M., Chaston, C. C., Hatch, S. M., Livadiotis, G., et al. (2018). Electron power-law spectra in solar and space plasmas. *Space Science Reviews*, *214*, 82. https://doi.org/10.1007/s11214-018-0515-4

Olsen, N., Albini, G., Bouffard, J., et al. (2020). Magnetic observations from CryoSat-2: Calibration and processing of satellite platform magnetometer data. *Earth Planets and Space*, *72*, 48. https://doi.org/10.1186/s40623-020-01171-9

Park, I., Miyoshi, Y., Mitani, T., Hori, T., Takashima, T., Kurita, S., et al. (2018). Energetic electron flux variations of the outer radiation belt during magnetic storms observed by Arase/HEP - Calibration of the instrument using Geant4 and superposed epoch analysis, American Geophysical Union, Fall Meeting 2018, abstract #SM33B-3559, 2018AGUFMSM33B3559P.

Pierrard, V., Ripoll, J.-F., Cunningham, G., Botek, E., Santolik, O., Thaller, S., et al. (2021). Observations and simulations of dropout events and flux decays in October 2013: Comparing MEO equatorial with LEO polar orbit. *Journal of Geophysical Research: Space Physics*, *126*, e2020JA028850

Reeves, G. D., Larsen, B., Skoug, R., Funsten, H., Claudepierre, S., Fennell, J., et al. (2016). Energy dependent dynamics of keV to MeV electrons in the inner zone, outer zone, and slot regions. *Journal of Geophysical Research: Space Physics*, *121*, 397–412. https://doi.org/10.1002/2015JA021569

Reidy, J. A., Horne, R. B., Glauert, S. A., Clilverd, M. A., Meredith, N. P., Woodfield, E. E., et al. (2021). Comparing electron precipitation fluxes calculated from pitch angle diffusion coefficients to LEO satellite observations. *Journal of Geophysical Research: Space Physics*, *126*, e2020JA028410. https://doi.org/10.1029/2020JA028410

Ripoll, J.-F., Reeves, G. D., Cunningham, G. S., Loridan, V., Denton, M., Santolik, O., et al. (2016). Reproducing the observed energy-dependent structure of Earth's electron radiation belts during storm recovery with an event-specific diffusion model. *Geophysical Research Letters*, *43*, 5616–5625. https://doi.org/10.1002/2016GL068869

Rodger, C. J., Carson, B. R., Cummer, S. A., Gamble, R. J., Clilverd, M. A., Green, J. C., et al. (2010). Contrasting the efficiency of radiation belt losses caused by ducted and nonducted whistler-mode waves from ground-based transmitters. *Journal of Geophysical Research*, *115*, A12208. https://doi.org/10.1029/2010JA015880

Rodger, C. J., Clilverd, M. A., Green, J. C., & Lam, M. M. (2010). Use of POES SEM-2 observations to examine radiation belt dynamics and energetic electron precipitation into the atmosphere. *Journal of Geophysical Research*, *115*, A04202. https://doi.org/10.1029/2008JA014023

Sauvaud, J. A., Moreau, T., Maggiolo, R., Treilhou, J. P., Jacquey, C., Cros, A., et al. (2006). High-energy electron detection onboard DEMETER: The IDP spectrometer, description and first results on the inner belt. *Planetary and Space Science*, *54*(5), 502–511. https://doi.org/10.1016/j.pss.2005.10.019

Selesnick, R. S. (2015). Measurement of inner radiation belt electrons with kinetic energy above 1 MeV. *Journal of Geophysical Research: Space Physics*, *120*, 8339–8349. https://doi.org/10.1002/2015JA021387

Seo, H., Shin, Y., Ju, W., Seol, W., Lee, C., Lee, C., et al. (2021). Medium energy charged particle detector with a deflecting electrostatic field for measurement of suprathermal electrons, protons, and neutrals aboard next-generation small satellite-1. *Advances in Space Research*, *68*(4), 1998–2021. https://doi.org/10.1016/j.asr.2021.04.031

Seo, Y., Yoon, S., Woo, J., Seon, J., Sohn, J., Min, K.-W., et al. (2015). The medium energy particle detector in the range of 20-400 keV for the study of space storm on NEXTSAT-1. *Aeronautics, Nano, Bio, Robotics. Energy*, *15*, 25–28.

Shin, D.-K., Lee, D.-Y., Kim, J.-H., & Cho, J.-H. (2014). Prediction model of the outer radiation belt developed by Chungbuk National University. *Journal of Astronomy and Space Sciences*, *31*(4), 303–309. https://doi.org/10.5140/jass.2014.31.4.303

Sohn, J., Lee, J., Min, K., Lee, J., Lee, S., et al. (2018). HEPD on NEXTSat-1: A high energy particle detector for measurements of precipitating radiation belt electrons. *Journal of the Korean Physical Society*, *72*, 1086–1093. https://doi.org/10.3938/jkps.72.1086

Søraas, F., Sandanger, M. I., & Smith-Johnsen, C. (2018). NOAA POES and MetOp particle observations during the 17 March 2013 storm. *Journal of Atmospheric and Solar-Terrestrial Physics*, *177*, 115–124. https://doi.org/10.1016/j.jastp.2017.09.004

Stolle, C., Michaelis, I., Xiong, C., Rother, M., Usbeck, T., Yamazaki, Y., et al. (2021). Observing Earth's magnetic environment with the GRACE-FO mission. *Earth Planets and Space*, *73*, 51. https://doi.org/10.1186/s40623-021-01364-w

Suvorova, A. V. (2017). Flux enhancements of >30 keV electrons at low drift shells L < 1.2 during last solar cycles. *Journal of Geophysical Research: Space Physics*, *122*, 12274–12287. https://doi.org/10.1002/2017JA024556

Turner, D. L., Claudepierre, S. G., Fennell, J. F., O'Brien, T. P., Blake, J. B., Lemon, C., et al. (2015). Energetic electron injections deep into the inner magnetosphere associated with substorm activity. *Geophysical Research Letters*, *42*, 2079–2087. https://doi.org/10.1002/2015GL063225

Van Allen, J. A., & Frank, L. A. (1959). Radiation around the Earth to a radial distance of 107,400 km. *Nature*, *183*, 430–434. https://doi.org/10.1038/183430a0

van de Kamp, M., Rodger, C. J., Seppälä, A., Clilverd, M. A., & Verronen, P. T. (2018). An updated model providing long-term data sets of energetic electron precipitation, including zonal dependence. *Journal of Geophysical Research: Atmospheres*, *123*, 9891–9915. https://doi.org/10.1029/2017JD028253

Whittaker, I. C., Gamble, R. J., Rodger, C. J., Clilverd, M. A., & Sauvaud, J.-A. (2013). Determining the spectra of radiation belt electron losses: Fitting DEMETER electron flux observations for typical and storm times. *Journal of Geophysical Research: Space Physics*, *118*, 7611–7623. https://doi.org/10.1002/2013JA019228

Whittaker, I. C., Rodger, C. J., Clilverd, M. A., & Sauvaud, J.-A. (2014). The effects and correction of the geometric factor for the POES/MEPED electron flux instrument using a multisatellite comparison. *Journal of Geophysical Research: Space Physics*, *119*, 6386–6404. https://doi.org/10.1002/2014JA020021

Xiang, Z., Ni, B., Zhou, C., Zou, Z., Gu, X., Zhao, Z., et al. (2016). Multi-satellite simultaneous observations of magnetopause and atmospheric losses of radiation belt electrons during an intense solar wind dynamic pressure pulse. *Annales Geophysicae*, *34*, 493–509. https://doi.org/10.5194/angeo-34-493-2016

Yang, X., Ni, B., Yu, J., Zhang, Y., Zhang, X., & Sun, Y. (2017). Unusual refilling of the slot region between the Van Allen radiation belts from November 2004 to January 2005. *Journal of Geophysical Research: Space Physics*, *122*, 6255–6270. https://doi.org/10.1002/2016JA023204

Yoo, J.-H., Lee, D.-Y., Kim, E.-J., Seo, H., Ryu, K., Kim, K.-C., et al. (2021). A substorm injection event and the radiation belt structure observed by space radiation detectors onboard NEXTSat-1. *Journal of Astronomy and Space Sciences*, *38*(1), 31–38. https://doi.org/10.5140/JASS.2021.38.1.31

Zhao, H., Johnston, W. R., Baker, D. N., Li, X., Ni, B., Jaynes, A. N., et al. (2019). Characterization and evolution of radiation belt electron energy spectra based on the Van Allen Probes measurements. *Journal of Geophysical Research: Space Physics*, *124*, 4217–4232. https://doi.org/10.1029/2019JA026697